

Floquet topological phases in a spin-1/2 double kicked rotor

Longwen Zhou* and Jiangbin Gong†

Department of Physics, National University of Singapore, Singapore 117551, Republic of Singapore

(Dated: 2018-03-08)

The double kicked rotor model is a physically realizable extension of the paradigmatic kicked rotor model in the study of quantum chaos. Even before the concept of Floquet topological phases became widely known, the discovery of the Hofstadter butterfly spectrum in the double kicked rotor model [J. Wang and J. Gong, Phys. Rev. A **77**, 031405 (2008)] already suggested the importance of periodic driving to the generation of unconventional topological matter. In this work, we explore Floquet topological phases of a double kicked rotor with an *extra* spin-1/2 degree of freedom. The latter has been experimentally engineered in a quantum kicked rotor recently by loading ^{87}Rb condensates into a periodically pulsed optical lattice. Under the on-resonance condition, the spin-1/2 double kicked rotor admits fruitful topological phases due to the interplay between its external and internal degrees of freedom. Each of these topological phases is characterized by a pair of winding numbers, whose combination predicts the number of topologically protected 0 and π -quasienergy edge states in the system. Topological phases with arbitrarily large winding numbers can be easily found by tuning the kicking strength. We discuss an experimental proposal to realize this model in kicked ^{87}Rb condensates, and suggest to detect its topological invariants by measuring the mean chiral displacement in momentum space.

I. INTRODUCTION

A topological characterization of a quantum chaos model by Leboeuf *et al* [1] pioneered the use of periodic driving fields to create topological phases of matter absent in time-independent systems. The model proposed in Ref. [1] was however rather abstract because it is quantized on a phase space torus. By extending the paradigmatic kicked rotor model in the study of quantum chaos [2–10], Wang and Gong proposed a physically realizable double kicked rotor model [11] and discovered Hofstadter’s butterfly-like Floquet spectrum therein [12]. This finding strongly suggested that such periodically driven systems are topologically rich and should be highly useful as dynamical systems to explore condensed-matter physics. Indeed, the work by Wang and Gong [11] has led to the proposal of a topological Thouless pump in momentum space [13], the proof of the topological equivalence between the double kicked rotor model and the kicked Harper model [14–16], and the identification of many topological edge states in both of the two models [17].

To date, Floquet topological states of matter have been well recognized as a promising concept and a fruitful topic. Floquet states, being intrinsically out-of-equilibrium, can be engineered to carry topological properties that are either analogous to [18–30], or even beyond their static cousins [31–42]. The latter includes, but is not limited to, degenerate π -quasienergy edge states [32–34], counterpropagating [35–37] and anomalous chiral edge states [38, 39] in both insulating [40] and superconducting [41] band structures, leading to new types of topological classification schemes and bulk-boundary relations [42–46]. Accompanying great theoretical efforts in exploring these intriguing features [47], Floquet topological states have also been observed in several experimental settings, including ultracold atom [48], photonic [49–51], phononic and acoustic systems [52].

Motivated by recent experimental advances, here we continue to explore Floquet topological phases in the context of double kicked rotor model. The Hamiltonian of an earlier quantum double kicked rotor (DKR) [11] model, which was realized by cold atoms subjected to pairs of pulses in an optical lattice [53], is given by

$$\hat{H} = \frac{\hat{p}^2}{2} + \kappa_1 \cos(\hat{x}) \sum_m \delta(t - mT) + \kappa_2 \cos(\hat{x} + \beta) \sum_m \delta(t - mT - \tau). \quad (1)$$

The stroboscopic dynamics of the system is governed by its evolution operator over one δ -kicking period T , *i.e.*, the Floquet operator

$$\hat{F} = e^{-i(T-\tau)\frac{\hat{p}^2}{2\hbar}} e^{-i\frac{\kappa_2}{\hbar} \cos(\hat{x}+\beta)} e^{-i\tau\frac{\hat{p}^2}{2\hbar}} e^{-i\frac{\kappa_1}{\hbar} \cos(\hat{x})}. \quad (2)$$

Here all quantities are in dimensionless units. \hat{x} and \hat{p} are position and momentum operators for cold atoms. β is the phase shift between two kicking optical lattice potentials of strengths κ_1 and κ_2 , separated by a time delay $\tau \in (0, T)$. Due to the spatial periodicity of kicking potentials, the momentum \hat{p} take values $p = (n + \eta)\hbar$, where $\eta \in (0, 1)$ is the conserved quasimomentum and $n \in \mathbb{Z}$. For a Bose-Einstein condensate (BEC) of large coherence width [8, 54], η can be set to zero, and $\hat{p} = \hbar\hat{n}$ only takes integer multiples of Planck constant \hbar . Then under the on-resonance condition [8, 9, 54] $\hbar T = 4\pi$, the quantum DKR has a Hofstadter’s butterfly-like quasienergy spectrum [12], characterized by fruitful topological band/gap structures and consecutive topological phase transitions versus the change of the system’s effective Planck constant \hbar [11].

In this work, we take one step further in the study of DKR by considering an internal spin-1/2 degree of freedom. The Floquet operator of such a spin-1/2 double kicked rotor (DKRS) is given by

$$\hat{U} = e^{-i(T-\tau)\frac{\hat{p}^2}{2\hbar}} e^{-i\frac{\kappa_2}{\hbar} \cos(\hat{x}+\beta)\sigma_y} e^{-i\tau\frac{\hat{p}^2}{2\hbar}} e^{-i\frac{\kappa_1}{\hbar} \cos(\hat{x})\sigma_x}, \quad (3)$$

where $\sigma_{x,y,z}$ are Pauli matrices acting on internal spin space

* zhoulw13@u.nus.edu

† phygj@nus.edu.sg

of the rotor. More specifically, in the case of quasimomentum $\eta = 0$ [8, 54], time delay $\tau = T/2$, and under on-resonance condition [10, 54] $\hbar\tau = 4\pi$, the Floquet propagator of DKRS reduces to

$$\hat{U} = e^{-iK_2 \cos(\hat{x}+\beta)\sigma_y} e^{-iK_1 \cos(\hat{x})\sigma_x}, \quad (4)$$

where $K_{1,2} = \kappa_{1,2}/\hbar$ are rescaled kicking strengths. In the following, we will first discuss a possible way of engineering the on-resonance DKRS (ORDKRS) described by Eq. (4) in a periodically pulsed BEC, thanks to a recent experimental realization of quantum walks in momentum space [55, 56]. Next, we will explore the rich topological phases of ORDKRS. Finally, we suggest to probe bulk topological invariants of ORDKRS by measuring the mean chiral displacement of a wave packet over tens of kicks, which is also experimentally available in both photonic [58] and cold atom [59] systems.

II. REALIZATION OF THE ORDKRS

The formalism of ORDKRS as described by Eq. (4) is inspired by a recent experiment, which realizes discrete time quantum walks in momentum space with a BEC of ^{87}Rb [55, 56]. The experimental platform is sketched in Fig. 1 of Ref. [55]. Each step of the quantum walk is composed of two consecutive operations. First, a resonant microwave is applied to the ^{87}Rb condensate, which introduces a rotation within the two-state space of its ground hyperfine levels $5^2S_{1/2}F = 1$ and $5^2S_{1/2}F = 2$. This realizes a ‘‘coin toss’’ described by [55, 56]

$$\mathcal{M}(\alpha, \chi) = e^{-i\frac{\alpha}{2}[\sin(\chi)\sigma_x - \cos(\chi)\sigma_y]}, \quad (5)$$

where $\sigma_{x,y,z}$ are Pauli matrices acting on the internal two-state space, and the rotation angles α, χ are controllable experimentally. Next, the BEC is subjected to a short laser pulse, whose frequency is detuned from the frequency between the two hyperfine levels, realizing the far off-resonant condition and producing periodic potentials. This step employs the atom-optical realization of the quantum kicked rotor (ratchet accelerator) with a kicking strength $k = \frac{\Omega^2 \tau_p}{\Delta}$, where Ω is the Rabi frequency, τ_p is the pulse length, and Δ is the detuning of laser light from the atomic transition. Notably, the detuning Δ is positive for the state $5^2S_{1/2}F = 1$ and negative for the state $5^2S_{1/2}F = 2$ of ^{87}Rb . Then under the quantum on-resonance condition [55, 56] (corresponding to the choice $\hbar\tau = 4\pi$ in our model), the second operation in a quantum walk step is described by a propagator [57]

$$\mathcal{T} = e^{-iK \cos(\hat{x})\sigma_z}, \quad (6)$$

where $K = \frac{\Omega^2 \tau_p}{|\Delta|}$ is the absolute value of kicking strength. The coupling between the internal degrees of freedom (hyperfine levels $F = 1, 2$) and the external motion (hopping in momentum space) is realized by the term $\cos(\hat{x})\sigma_z$.

The successful implementations of ‘‘coin toss’’ operation $\mathcal{M}(\alpha, \chi)$ and spin-dependent walk \mathcal{T} in kicked BECs set the starting point for the realization of an ORDKRS as described

by Eq. (4). To see this, we rewrite the Floquet operator of ORDKRS as

$$\hat{U} = \hat{V}_2 \hat{V}_1, \quad (7)$$

where $\hat{V}_1 = e^{-iK_1 \cos(\hat{x})\sigma_x}$ and $\hat{V}_2 = e^{-iK_2 \cos(\hat{x}+\beta)\sigma_y}$. Then each of these two propagators can be realized by proper combinations of ‘‘coin toss’’ and spin-dependent walk operations:

$$\hat{V}_1 = e^{-iK_1 \cos(\hat{x})\sigma_x} = \mathcal{M}\left(-\frac{\pi}{2}, 0\right) \mathcal{T}_1 \mathcal{M}\left(\frac{\pi}{2}, 0\right), \quad (8)$$

$$\hat{V}_2 = e^{-iK_2 \cos(\hat{x}+\beta)\sigma_y} = \mathcal{M}\left(-\frac{\pi}{2}, \frac{\pi}{2}\right) \mathcal{T}_2 \mathcal{M}\left(\frac{\pi}{2}, \frac{\pi}{2}\right), \quad (9)$$

where $\mathcal{T}_1 = e^{-iK_1 \cos(\hat{x})\sigma_z}$ and $\mathcal{T}_2 = e^{-iK_2 \cos(\hat{x}+\beta)\sigma_z}$ are two spin-dependent walks. The different kicking strengths $K_{1,2} = \Omega_{1,2}^2 \tau_p / |\Delta_{1,2}|$ may be realized by letting the two walks to have either a different Rabi frequency $\Omega_1 \neq \Omega_2$ or a different detuning $|\Delta_1| \neq |\Delta_2|$. Putting together, the Floquet operator of ORDKRS is realized by a sequence of operations as $\hat{U} = \mathcal{M}\left(-\frac{\pi}{2}, \frac{\pi}{2}\right) \mathcal{T}_2 \mathcal{M}\left(\frac{\pi}{2}, \frac{\pi}{2}\right) \mathcal{M}\left(-\frac{\pi}{2}, 0\right) \mathcal{T}_1 \mathcal{M}\left(\frac{\pi}{2}, 0\right)$. Since each sub-step in this sequence is already realized in the quantum walk experiment of ^{87}Rb condensates [55, 56], the realization of ORDKRS as described by Eq. (4) should already be available in the same experimental setup or other similar platforms.

To further motivate experimental interests, we will analyze the topological properties of ORDKRS in the following sections. To be more explicit, we choose the phase shift between the two kicks to be $\beta = -\frac{\pi}{2}$ in Eq. (4). This gives us the following Floquet operator of an ORDKRS:

$$\hat{U}_R = e^{-iK_2 \sin(\hat{x})\sigma_y} e^{-iK_1 \cos(\hat{x})\sigma_x}. \quad (10)$$

As will be shown, this system possesses a fruitful Floquet topological phases, with their topological winding numbers detectable by measuring momentum distributions of the system over tens of driving periods.

Note in passing that by choosing the initial state to be a coherent superposition of several momentum eigenstates [55, 56], the Floquet operator \hat{U}_R may also be used to engineer a split step quantum walk in the momentum space of BECs, whose topological properties have been thoroughly explored in previous studies [60]. Compared with the split step quantum walk, the ORDKRS introduced here admits a richer topological phase diagram, with the possibility to access phases with large topological invariants.

III. TOPOLOGICAL PHASES OF THE ORDKRS

Similar to their static cousins [61], single-particle Floquet topological phases in one-dimension are all symmetry protected [45]. The Floquet operator \hat{U}_R , as defined in Eq. (10), possesses a chiral symmetry. Its topological phases are then characterized by a pair of integers ($\mathbb{Z} \times \mathbb{Z}$), defined in two complementary chiral symmetric time frames [43]. These integers predict the number of degenerate 0 and π -quasienergy edge states in the two spectrum gaps of \hat{U}_R , respectively. These

will be demonstrated in the following subsections.

A. Chiral symmetric time frame and topological winding number

The chiral symmetry of \hat{U}_R is most clearly seen by transforming it into two chiral symmetric time frames [43], in which it has the following forms:

$$\hat{U}_1 = e^{-i\frac{K_1}{2} \cos(\hat{x})\sigma_x} e^{-iK_2 \sin(\hat{x})\sigma_y} e^{-i\frac{K_1}{2} \cos(\hat{x})\sigma_x}, \quad (11)$$

$$\hat{U}_2 = e^{-i\frac{K_2}{2} \sin(\hat{x})\sigma_y} e^{-iK_1 \cos(\hat{x})\sigma_x} e^{-i\frac{K_2}{2} \sin(\hat{x})\sigma_y}. \quad (12)$$

It is seen that both \hat{U}_1 and \hat{U}_2 are related to \hat{U}_R by unitary transformations, meaning that they all share the same Floquet quasienergy spectrum. Furthermore, both \hat{U}_1 and \hat{U}_2 possess the chiral symmetry as

$$\Gamma \hat{U}_1 \Gamma = \hat{U}_1^\dagger, \quad \Gamma \hat{U}_2 \Gamma = \hat{U}_2^\dagger, \quad \Gamma = \sigma_z. \quad (13)$$

Here the chiral symmetry operator Γ is both Hermitian and unitary, *i.e.*, $\Gamma = \Gamma^\dagger = \Gamma^{-1}$. Based on the periodic table of Floquet topological states [45], each phase of \hat{U}_R is then characterized by a pair of integer winding numbers $(W_0, W_\pi) \in \mathbb{Z} \times \mathbb{Z}$ [43], given by

$$W_0 = \frac{W_1 + W_2}{2}, \quad W_\pi = \frac{W_1 - W_2}{2}, \quad (14)$$

where W_1 and W_2 are winding numbers of Floquet operators \hat{U}_1 and \hat{U}_2 , respectively. The winding numbers (W_0, W_π) allow us to achieve a full classification of the topological phases of \hat{U}_R , as will be discussed in Sec. III B.

To compute these winding numbers for each Floquet topological phase, we rewrite \hat{U}_ℓ ($\ell = 1, 2$) by combining its three pieces. In the position representation $\{|\theta\rangle | \theta \in [-\pi, \pi]\}$, we then have $\hat{U}_\ell = \sum_\theta |\theta\rangle \langle \theta| e^{-iE(\theta)\mathbf{n}_\ell \cdot \boldsymbol{\sigma}}$. The dispersion $E(\theta)$ has the form (see Appendix A for more details)

$$E(\theta) = \arccos[\cos(\mathcal{K}_1) \cos(\mathcal{K}_2)], \quad (15)$$

where $\mathcal{K}_1 \equiv K_1 \cos \theta$ and $\mathcal{K}_2 \equiv K_2 \sin \theta$. The vector of matrix $\boldsymbol{\sigma} = (\sigma_x, \sigma_y)$, and the two-component unit vectors $\mathbf{n}_\ell = (n_{\ell x}, n_{\ell y})$ for $\ell = 1, 2$ are explicitly given by

$$n_{1x} = \frac{\sin(\mathcal{K}_1) \cos(\mathcal{K}_2)}{\sqrt{\sin^2(\mathcal{K}_1) \cos^2(\mathcal{K}_2) + \sin^2(\mathcal{K}_2)}}, \quad (16)$$

$$n_{1y} = \frac{\sin(\mathcal{K}_2)}{\sqrt{\sin^2(\mathcal{K}_1) \cos^2(\mathcal{K}_2) + \sin^2(\mathcal{K}_2)}}, \quad (17)$$

and

$$n_{2x} = \frac{\sin(\mathcal{K}_1)}{\sqrt{\sin^2(\mathcal{K}_1) \cos^2(\mathcal{K}_2) + \sin^2(\mathcal{K}_2)}}, \quad (18)$$

$$n_{2y} = \frac{\sin(\mathcal{K}_2) \cos(\mathcal{K}_1)}{\sqrt{\sin^2(\mathcal{K}_1) \cos^2(\mathcal{K}_2) + \sin^2(\mathcal{K}_2)}}, \quad (19)$$

Using these vectors, the winding number W_ℓ of Floquet operator \hat{U}_ℓ [58] can be computed as

$$W_\ell = \int_{-\pi}^{\pi} \frac{d\theta}{2\pi} (\mathbf{n}_\ell \times \partial_\theta \mathbf{n}_\ell)_z, \quad \ell = 1, 2. \quad (20)$$

As evidenced by this expression, the winding number W_ℓ counts the number of times that the unit vector \mathbf{n}_ℓ rotates around the z -axis when θ changes over a period from $-\pi$ to π . Thanks to the chiral symmetry of \hat{U}_ℓ , the vector \mathbf{n}_ℓ is constrained to rotate on the x - y plane, ensuring W_ℓ to be a well defined integer. Furthermore, the quantization of the winding number W_ℓ is topologically protected, since W_ℓ cannot change its value under continuous deformations of the trajectory of \mathbf{n}_ℓ on the x - y plane. The topological property of winding numbers (W_0, W_π) are then carried over from winding numbers W_1 and W_2 through Eq. (14).

B. Topological phase diagram

If the trajectory of vector \mathbf{n}_ℓ on the x - y plane happens to pass through the origin of z -axis at some critical value $\theta = \theta_c$, the dispersion $E(\theta)$ will become gapless. This situation indicates the breakdown of the winding number definition (20) and the existence of a possible topological phase transition specified by its corresponding kicking strengths (K_{1c}, K_{2c}) . The collection of all these transition points on the plane of parameter space (K_1, K_2) forms the boundary between different Floquet topological phases of the ORDKRS.

To locate these phase boundaries, we note that being a phase factor defined modulus 2π , the dispersion $E(\theta)$ has in general two gaps at both quasienergies 0 and π , respectively. The closure of a spectrum gap in $E(\theta)$ then corresponds to either $E(\theta) = 0$ or $E(\theta) = \pi$, which means that $\cos(\mathcal{K}_1) \cos(\mathcal{K}_2) = \pm 1$ in Eq. (15), respectively. This condition can be met if and only if $K_1 \cos \theta = \mu\pi$ and $K_2 \sin \theta = \nu\pi$, where ν, μ are both integers. The combination of these conditions yields the following equation for the topological phase boundaries of \hat{U}_R :

$$\frac{\mu^2}{K_1^2} + \frac{\nu^2}{K_2^2} = \frac{1}{\pi^2}, \quad \mu, \nu \in \mathbb{Z}. \quad (21)$$

Following their experimental definitions, we focus on the regime of positive kicking strengths $K_1, K_2 > 0$. In this regime, the phase boundaries can be classified into three groups based on the value of integers (μ, ν) .

(i) $\mu = 0$: In this case, the phase boundaries $K_2 = \nu\pi$ ($\nu = 0, 1, 2, \dots$) are straight lines in parallel with the K_1 -axis

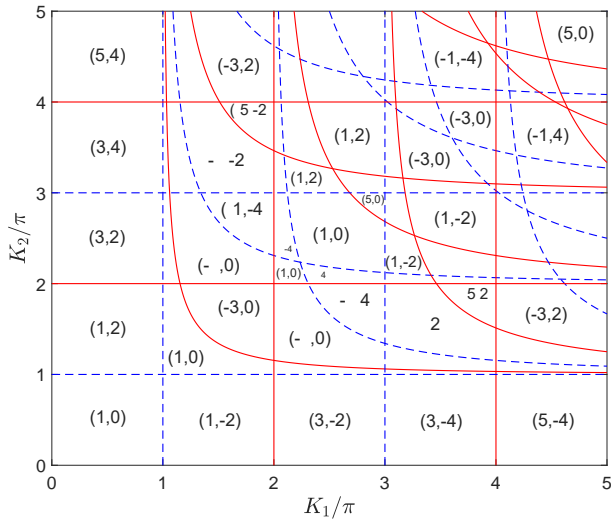


FIG. 1. (color online) Floquet topological phase diagram of the ORD-KRS \hat{U}_R versus kicking strengths (K_1, K_2) . Red solid (blue dashed) lines are phase boundaries, where the Floquet spectrum gap close at quasienergy 0 (π). Each closed patch corresponds to a unique topological phase, characterized by a pair of winding numbers (W_0, W_π) deduced from Eq. (14), as denoted in the figure for some representative phases.

on the K_1 - K_2 plane. Furthermore, when ν is an odd (even) integer, the Floquet spectrum gap will close at quasienergy π (0). The corresponding topological phase transition is only accompanied by the change of winding number W_π (W_0).

(ii) $\nu = 0$: In this case, the phase boundaries $K_1 = \mu\pi$ ($\mu = 0, 1, 2, \dots$) are straight lines in parallel with the K_2 -axis on the K_1 - K_2 plane. Furthermore, when μ is an odd (even) integer, the Floquet spectrum gap will close at quasienergy π (0). The corresponding topological phase transition is only accompanied by the change of winding number W_π (W_0).

(iii) $\mu, \nu \neq 0$: In this case, the phase boundary curves are described by the equation $\frac{K_2}{\pi} = \nu \left(1 - \frac{\mu^2}{K_1^2/\pi^2}\right)^{-1/2}$, with positive solutions only for $K_1 > \mu\pi$. Furthermore, when μ, ν have the opposite (same) parities, the Floquet spectrum gap will close at quasienergy π (0) along the phase boundary curve. The corresponding topological phase transition is only accompanied by the change of winding number W_π (W_0).

Combining points (i-iii) together with winding numbers calculated from Eq. (14), we are able to achieve a full topological classification of the ORD-KRS as described by the Floquet operator \hat{U}_R in Eq. (10). A topological phase diagram of the system up to $K_1 = K_2 = 5\pi$ is shown in Fig. 1. On the phase diagram, each closed patch is characterized by a pair of winding numbers (W_0, W_π) .

In Ref. [17], a phase diagram with similar phase boundaries is found in a spinless DKR model under a different on-resonance condition. Notably, the topological phase in each patch of that phase diagram is characterized by different winding numbers from that of the ORD-KRS studied here. This difference comes from distinct winding behaviors of the vector \mathbf{n}_l in the two models, even though they share the same Floquet

spectrum.

Furthermore, in the region $(K_1, K_2) \in (0, \pi) \times (0, \infty)$ ($(K_1, K_2) \in (0, \infty) \times (0, \pi)$), the winding numbers W_0 and W_π both tend to grow linearly along the direction of K_2 - (K_1 -)axis without bound (see Appendix. B for an illustration). This result mimics the change of quantum Hall resistance (here the winding number) with the increase of a magnetic field (here the kicking strength) in quantum Hall effects [5, 62]. A similar pattern is also observed in the phase diagram of the spinless DKR studied in Ref. [17]. The possibility of accessing phases with arbitrarily large winding numbers in the ORD-KRS makes it a good candidate to explore Floquet states and phase transitions in the regime of large topological invariants, which is usually absent in other experimentally realized one-dimensional Floquet systems like the split step quantum walk [60].

In the next subsection, we will explore the relation between the winding numbers of \hat{U}_R and the number of its topological edge states in a finite-size momentum space lattice.

C. Bulk-boundary correspondence

The Floquet operator $\hat{U}_R = e^{-iK_2 \sin(\hat{x})\sigma_y} e^{-iK_1 \cos(\hat{x})\sigma_x}$ can be written in momentum representation [17] as

$$\hat{U}_R = e^{-iK_2 \sum_n \frac{1}{2i} (n)\langle n+1 | -\text{h.c.} \rangle \sigma_y} e^{-iK_1 \sum_n \frac{1}{2} (n)\langle n+1 | +\text{h.c.} \rangle \sigma_x}, \quad (22)$$

where the momentum basis $\{|n\rangle | n \in \mathbb{Z}\}$ satisfies the eigenvalue equation $\hat{n}|n\rangle = n|n\rangle$, with \hat{n} being the dimensionless momentum operator as discussed in Sec. I. This result can be obtained, e.g., by first writing $K_1 \cos(\hat{x})\sigma_x$ in position representation as $K_1 \sum_\theta \frac{e^{i\theta} + e^{-i\theta}}{2} |\theta\rangle\langle\theta| \sigma_x$, and then performing a Fourier transform from position to momentum representation as $|\theta\rangle = \frac{1}{\sqrt{N}} \sum_{n=-\frac{N}{2}}^{\frac{N}{2}-1} e^{in\theta} |n\rangle$ under the periodic boundary condition $|n\rangle = |n+N\rangle$. Expressed in the form of Eq. (22), \hat{U}_R admits an interpretation of two consecutive kicks by momentum space tight-binding lattices on a spin-1/2 particle. If an open boundary condition can be introduced into this momentum space lattice, there will be topological edge states localized around its boundaries if the kicking strengths (K_1, K_2) reside in a topologically nontrivial patch of the phase diagram. This is guaranteed by the bulk-boundary correspondence of chiral symmetric Floquet systems [43]. More precisely, the absolute value of winding number W_0 (W_π) gives the number of degenerate edge state pairs at quasienergy 0 (π) in the momentum space lattice.

An illustration of this bulk-boundary relation is given in Fig. 2. The panel (a) of Fig. 2 shows the spectrum of \hat{U}_R at a fixed value of the first kicking strength $K_1 = 0.5\pi$ under open boundary conditions. With the change of the second kicking strength K_2 , the system undergoes two topological phase transitions, with quasienergy gap closing at π (0) for $K_2 = \pi$ ($K_2 = 2\pi$). These transitions separate the system in the considered range of parameters into three different topological phases, characterized by winding numbers $(W_0, W_\pi) = (1, 0)$, $(1, 2)$ and $(3, 2)$ (See also Fig. 1). These numbers correctly

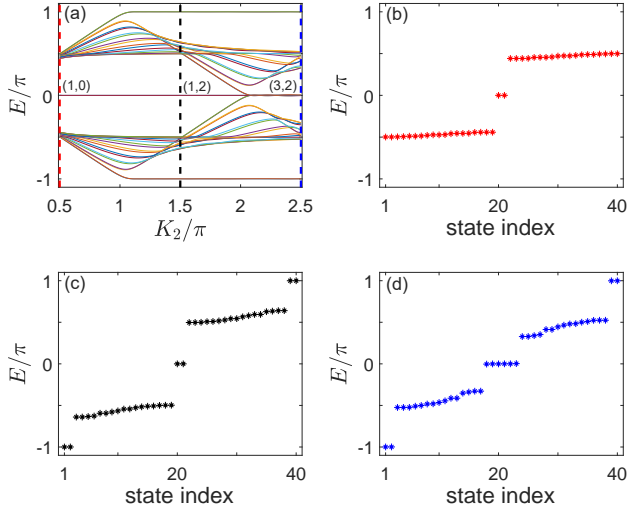


FIG. 2. (color online) Bulk-boundary correspondence of the ORD-KRS. Panel (a): Floquet spectrum E of \hat{U}_R versus K_2 at $K_1 = 0.5\pi$, for a momentum space lattice of $N = 20$ unit cells under open boundary conditions. Three topological phases with winding numbers $(W_0, W_\pi) = (1, 0)$, $(1, 2)$ and $(3, 2)$, as denoted on the figure, are separated by two transitions at $K_2 = \pi, 2\pi$. Panel (b): Floquet spectrum E at $K_2 = 0.5\pi$, referring to the cut along the red dashed line at the left end of Panel (a). There is a pair of 0-quasienergy edge states, corresponding to $W_0 = 1$. Panel (c): Floquet spectrum E at $K_2 = 1.5\pi$, referring to the cut along the black dashed line in the middle of Panel (a). There is a pair of 0- and two pairs of π -quasienergy edge states, corresponding to $W_0 = 1$ and $W_\pi = 2$. Panel (d): Floquet spectrum E at $K_2 = 2.5\pi$, referring to the cut along the blue dashed line at the right end of Panel (a). There are three pairs of 0- and two pairs of π -quasienergy edge states, corresponding to $W_0 = 3$ and $W_\pi = 2$.

predict the number of 0- and π -quasienergy edge state pairs in these three topological phases, as exemplified by panels (b) to (d) of Fig. 2. On the other hand, by counting the number of 0 and π edge state pairs in Fig. 2(b-d), we can also obtain the winding numbers (W_0, W_π) for each topological phases. This concludes the verification of bulk boundary correspondence in the chiral symmetric ORDKRS system.

As a notable feature of Fig. 2(a), there are regions in which the 0 and π quasienergy edge states coexist at the same system parameters [see Fig. 2(c) or 2(d) as an example]. In a recent study [63], it was shown that a superposition of 0 and π edge states form a new type of symmetry protected discrete time crystal phase, which is further used to propose a new approach to non-Abelian braiding and topological quantum computing in a superconducting Floquet system. The unbounded growth of winding numbers in the phase diagram Fig. 1 then implies the possibility of finding an arbitrarily large number of 0 and π quasienergy edge states at the same parameter of the ORD-KRS, and therefore the potential of engineering many different Floquet time crystal phases [64] in this system by superposing these edge states.

Experimentally, Floquet edge states between systems with different bulk topological properties have been observed in photonic quantum walks [49]. However, for the ORDKRS de-

fined in a momentum lattice as Eq. (22), it may not be easy to engineer a boundary between different momentum space regions. In the following section, we discuss an alternative way of detecting topological winding numbers of the ORDKRS by directly imaging the momentum distribution of a wave packet [59], which is available in kicked BEC experimental setups [55].

IV. PROBING BULK TOPOLOGICAL PROPERTIES OF THE ORDKRS

The topological winding numbers of a one-dimensional chiral symmetric system can be detected by measuring the mean chiral displacement (MCD) of a wave packet [58, 59]. Formally, it is the expectation value of chiral displacement operator $\hat{C}(t) = \hat{U}^\dagger(t)\hat{n}\Gamma\hat{U}(t)$ at some time t of the system's unitary evolution $\hat{U}(t)$. For the ORDKRS, \hat{n} and $\Gamma = \sigma_z$ represent the quantized momentum and chiral symmetry operators, respectively. Therefore the MCD of ORDKRS is just a signed momentum distribution, with the extra sign originating from the chiral symmetry. For the system of ^{87}Rb BECs prepared in the state $|\psi_0\rangle = |n=0, 5^2S_{1/2}F=1\rangle$ or $|n=0, 5^2S_{1/2}F=2\rangle$ of the $n=0$ -momentum sector at time $t=0$, the MCD after t driving periods reads

$$C_\ell(t) = \langle \psi_0 | \hat{U}_\ell^{-t} (\hat{n} \otimes \sigma_z) \hat{U}_\ell^t | \psi_0 \rangle, \quad (23)$$

where the Floquet operators \hat{U}_ℓ ($\ell = 1, 2$) are given by Eqs. (11) and (12). Further calculations lead to (see Appendix C for details):

$$C_\ell(t) = \frac{W_\ell}{2} - \int_{-\pi}^{\pi} \frac{d\theta}{2\pi} \frac{\cos[E(\theta)t]}{2} (\mathbf{n}_\ell \times \partial_\theta \mathbf{n}_\ell)_z \quad \ell = 1, 2. \quad (24)$$

Here W_ℓ is the winding number of \hat{U}_ℓ given by Eq. (20). The dispersion $E(\theta)$ is given by Eq. (15), and the components of unit vector \mathbf{n}_ℓ are given by Eqs. (16-19). As can be seen, $C_\ell(t)$ contains a time-independent topological part $\frac{W_\ell}{2}$ and an extra time-dependent oscillating term. For a not-too-flat dispersion $E(\theta)$, the oscillating term will tend to vanish for large t under the integral over θ . A bit more rigorously, the $C_\ell(t)$ averaged over t driving periods, *i.e.*,

$$\begin{aligned} \overline{C_\ell(t)} &\equiv \frac{1}{t} \sum_{t'=1}^t C_\ell(t') \\ &= \frac{W_\ell}{2} - \frac{1}{t} \sum_{t'=1}^t \int_{-\pi}^{\pi} \frac{d\theta}{2\pi} \frac{\cos[E(\theta)t']}{2} (\mathbf{n}_\ell \times \partial_\theta \mathbf{n}_\ell)_z, \end{aligned} \quad (25)$$

will gradually converge to half of the winding number W_ℓ with the increase of t . Once $\frac{W_1}{2}$ and $\frac{W_2}{2}$ are obtained from the time averaged MCD, the winding numbers (W_0, W_π) characterizing topological phases of the ORDKRS can be calculated by Eq. (14).

In Fig. 3, we present numerical results of $\overline{C_\ell(t)}$ along two different trajectories in the K_1 - K_2 parameter space, together with theoretical values of half winding numbers $W_1/2$ and

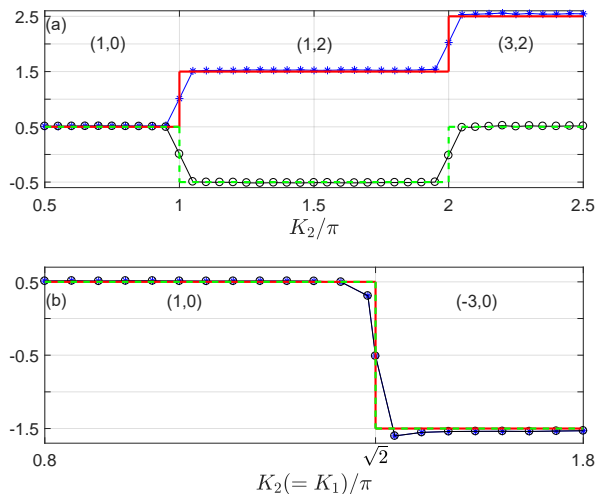


FIG. 3. (color online) Time averaged MCDs. Numerical values of $\overline{C_1(t)}$ and $\overline{C_2(t)}$, both averaged over $t = 20$ driving periods, are shown by blue stars and black circles. Theoretical values of half winding numbers $\frac{W_1}{2}$ and $\frac{W_2}{2}$ are shown by red solid and green dashed lines. In Panel (a), the kicking strength $K_1 = 0.5\pi$ and the three topological phases, separated by two transitions at $K_2 = \pi, 2\pi$, have winding numbers $(W_0, W_\pi) = \left(\frac{W_1+W_2}{2}, \frac{W_1-W_2}{2}\right) = (1, 0), (1, 2)$ and $(3, 2)$, as denoted in the figure. In Panel (b), the two topological phases separated by a transition at $K_1 = K_2 = \sqrt{2}\pi$ have winding numbers $(W_0, W_\pi) = \left(\frac{W_1+W_2}{2}, \frac{W_1-W_2}{2}\right) = (1, 0)$ and $(-3, 0)$, as denoted in the figure.

$W_2/2$. The numerical results at each set of kicking strengths (K_1, K_2) are obtained by directly evolving a wave packet, prepared at initial state $|n = 0, F = 1\rangle$ or $|n = 0, F = 2\rangle$, with propagators \hat{U}_1^t and \hat{U}_2^t in momentum space to find $C_1(t)$ and $C_2(t)$, respectively, and then averaging over the number of driving periods t . Up to $t = 20$, we find already very nice convergence of $\overline{C_\ell(t)}$ ($\ell = 1, 2$) to its corresponding half winding number $\frac{W_\ell}{2}$, with the error accounted for by the time-dependent term in Eq. (25). In the setup of ^{87}Rb BEC, an implementation of up to 50 kicks is mentioned to be experimentally available [55]. This corresponds to $t = 25$ driving periods in our double kicked rotor, more than the number needed to see a nice convergence in our numerical simulations.

Recently, the measurements of MCD have been achieved in both photonic [58] and cold atom [59] systems. In Ref. [58], the MCD is extracted from a quantum walk of twisted photons over 7 steps, and the measured results are robust to dynamical disorder. In Ref. [59], ^{87}Rb condensates are illuminated by a pair of off-resonant lasers to realize a synthetic lattice in momentum space. The coupling between adjacent momentum sites in this setup is controlled by two-photon Bragg transitions, and can be periodically quenched in time. In the high-frequency driving regime, the effective tight-binding Hamiltonian of the system falls into AIII or BDI topological class [61]. Disorder-induced topological phase transitions are then detected by measuring the MCD. Based on these facts, we believe that the realization of ORDKRS and measurements of its topological winding numbers are readily doable under cur-

rent experimental conditions.

V. CONCLUSIONS

In this work, we proposed a spin-1/2 on-resonance double kicked rotor model, which is realizable in BECs of ^{87}Rb subjected to pairs of periodic pulses by an optical lattice. The system owns many intriguing Floquet topological phases, each characterized by a pair of winding numbers and protected by the chiral symmetry of the Floquet operator. Using these winding numbers, a full topological phase diagram of the system was established. Under open boundary conditions, this pair of winding numbers could also predict the number of topologically protected edge state pairs at 0 and π -quasienergies of the Floquet spectrum. Finally, we proposed to detect these topological winding numbers by measuring the mean chiral displacement of a wave packet, initially localized at the center of the momentum space. The numerical values of mean chiral displacement, averaged over 20 kicking periods, tend to converge to the theoretical prediction of bulk winding numbers of the ORDKRS. Recently, the experimental measurements of mean chiral displacements have also been achieved in other model systems [58, 59].

Our choice of the on-resonance condition, *i.e.*, $\hbar\tau = 4\pi$ with $\tau = T/2$, makes the free evolution part of the Floquet operator to become an identity. Under more general resonance conditions, the free evolution part can also contribute to the dynamics. The resulting Floquet operators could then possess more than two Floquet bands and different types of topological phases, as already indicated in a previous study of the spinless quantum DKR [17]. Exploring the impact of an extra spin degree of freedom on the topological phases of the DKR under general resonance conditions is an interesting topic for future study.

Due to experimental constraints on the detection window of momentum states, only small to intermediate values of kicking strength are considered in our numerical simulations. When the kicking strength is large, the dynamics of the spin-1/2 double kicked rotor will in general become chaotic in its classical limit. Exploring quantum dynamics and its possible topological signatures in this classically chaotic regime is certainly an intriguing topic. A recent study found that up to large enough kicking strengths, the winding numbers W of a periodically quenched chiral symmetric Floquet system satisfy a Gaussian distribution around $W = 0$ [65]. Initial numerical calculations in our system suggest a similar pattern along the line $K_2 = \lambda K_1$ on the phase diagram for any $|\lambda| \in (0, \infty)$. However, for trajectories parallel to K_1 or K_2 axis on the phase diagram and constrained within $K_2 \in (0, \pi)$ or $K_1 \in (0, \pi)$ regions, respectively, the winding numbers W change monotonically with the kicking strength and satisfy instead a uniform distribution. The qualitative difference between these two types of winding number distributions, the transition between them, and its possible connection to the quantum-to-classical transitions in ORDKRS also deserve further explorations.

Finally, the effect of disorder on Floquet topological phases is of great theoretical and experimental interests [28, 38, 58,

59]. In a chiral symmetric system realized by quantum walk of twisted photons, the Floquet topological phases have been demonstrated to be robust to weak temporal disorder [58]. Furthermore, disorder induced transitions from topological Anderson insulator to normal insulator phases, and even the reverse, have also been observed quite recently in the momentum space of laser driven ultracold atoms [59]. One limitation of the models explored in these experiments is that their winding numbers cannot be larger than one. On the contrary, the spin-1/2 double kicked rotor proposed in this work allows topological phases with arbitrarily large winding numbers to appear. The realization of ORDKRS should then open the door for experimental explorations of the interplay between disorder and Floquet topological phases in large topological invariant regimes, resulting in potentially more fruitful patterns of Floquet topological Anderson transitions.

ACKNOWLEDGEMENT

J.G. is supported by the Singapore NRF grant No. NRF-NRFI2017-04 (WBS No. R-144-000-378-281) and the Singapore Ministry of Education Academic Research Fund Tier I (WBS No. R-144-000-353-112).

Appendix A: Expression of \hat{U}_ℓ in position representation

In this appendix, we expand a bit more on the derivation of \hat{U}_ℓ ($\ell = 1, 2$) in the two symmetric time frames used in the main text. In position representation, the Floquet operator \hat{U}_ℓ in symmetric time frame ℓ is written as $\hat{U}_\ell = \sum_\theta |\theta\rangle\langle\theta| U_\ell(\theta)$, with

$$U_1(\theta) = e^{-i\frac{\mathcal{K}_1}{2}\sigma_x} e^{-i\mathcal{K}_2\sigma_y} e^{-i\frac{\mathcal{K}_1}{2}\sigma_x}, \quad (\text{A.1})$$

$$U_2(\theta) = e^{-i\frac{\mathcal{K}_2}{2}\sigma_y} e^{-i\mathcal{K}_1\sigma_x} e^{-i\frac{\mathcal{K}_2}{2}\sigma_y}, \quad (\text{A.2})$$

where $\mathcal{K}_1 = K_1 \cos \theta$ and $\mathcal{K}_2 = K_2 \sin \theta$ as defined in the main text. Using the formula $e^{-i\gamma \mathbf{n} \cdot \boldsymbol{\sigma}} = \cos(\gamma) - i \sin(\gamma) \mathbf{n} \cdot \boldsymbol{\sigma}$, with $\boldsymbol{\sigma} = (\sigma_x, \sigma_y, \sigma_z)$ and \mathbf{n} being a unit vector, we can reorganize $U_1(\theta)$ and $U_2(\theta)$ as

$$U_1(\theta) = \cos(\mathcal{K}_1) \cos(\mathcal{K}_2) - i[\sin(\mathcal{K}_1) \cos(\mathcal{K}_2) \sigma_x + \sin(\mathcal{K}_2) \sigma_y], \quad (\text{A.3})$$

$$U_2(\theta) = \cos(\mathcal{K}_1) \cos(\mathcal{K}_2) - i[\sin(\mathcal{K}_1) \sigma_x + \sin(\mathcal{K}_2) \cos(\mathcal{K}_1) \sigma_y]. \quad (\text{A.4})$$

With the identifications

$$\cos(E) = \cos(\mathcal{K}_1) \cos(\mathcal{K}_2), \quad (\text{A.5})$$

$$\begin{aligned} \sin(E) &= \sqrt{\sin^2(\mathcal{K}_1) \cos^2(\mathcal{K}_2) + \sin^2(\mathcal{K}_2)}, \\ &= \sqrt{\sin^2(\mathcal{K}_1) + \sin^2(\mathcal{K}_2) \cos^2(\mathcal{K}_1)}, \end{aligned} \quad (\text{A.6})$$

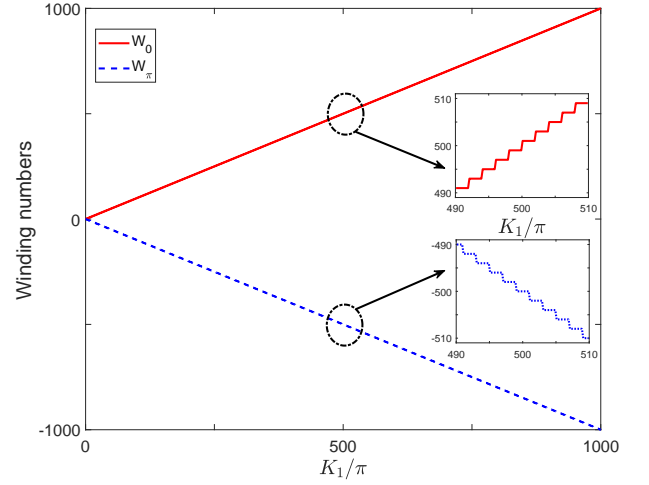


FIG. B.1. (color online) The linear growth of winding numbers (W_0, W_π) versus kicking strength K_1 at a fixed kicking strength $K_2 = 0.5\pi$.

where E being the dispersion relation, and

$$n_{1x} = \frac{\sin(\mathcal{K}_1) \cos(\mathcal{K}_2)}{\sin(E)}, \quad n_{1y} = \frac{\sin(\mathcal{K}_2)}{\sin(E)}, \quad (\text{A.7})$$

$$n_{2x} = \frac{\sin(\mathcal{K}_1)}{\sin(E)}, \quad n_{2y} = \frac{\sin(\mathcal{K}_2) \cos(\mathcal{K}_1)}{\sin(E)}, \quad (\text{A.8})$$

we can further express $U_1(\theta)$ and $U_2(\theta)$ as

$$\begin{aligned} U_\ell(\theta) &= \cos(E) - i \sin(E) (n_{\ell x} \sigma_x + n_{\ell y} \sigma_y) \\ &= e^{-iE(\theta)(n_{\ell x} \sigma_x + n_{\ell y} \sigma_y)} \quad \ell = 1, 2 \end{aligned} \quad (\text{A.9})$$

Finally, identifying the unit vector $\mathbf{n}_\ell = (n_{\ell x}, n_{\ell y})$ for $\ell = 1, 2$, we arrive at the expression $\hat{U}_\ell = \sum_\theta |\theta\rangle\langle\theta| e^{-iE(\theta) \mathbf{n}_\ell \cdot \boldsymbol{\sigma}}$ used in the main text.

Appendix B: Linear growth of winding numbers

In this appendix, we give an illustration for the change of winding numbers (W_0, W_π) along a trajectory in parallel with the K_1 -axis at a fixed $K_2 \in (0, \pi)$ in the phase diagram Fig. 1. From Eq. (20), the winding numbers W_1, W_2 of Floquet operators \hat{U}_1, \hat{U}_2 defined in Eqs. (11,12) are given by

$$W_1 = \int_{-\pi}^{\pi} \frac{d\theta}{2\pi} \frac{\sin(\mathcal{K}_1) \partial_\theta \mathcal{K}_2 - \sin(\mathcal{K}_2) \cos(\mathcal{K}_1) \cos(\mathcal{K}_2) \partial_\theta \mathcal{K}_1}{\sin^2(E)}, \quad (\text{B.1})$$

$$W_2 = \int_{-\pi}^{\pi} \frac{d\theta}{2\pi} \frac{\sin(\mathcal{K}_1) \cos(\mathcal{K}_1) \cos(\mathcal{K}_2) \partial_\theta \mathcal{K}_2 - \sin(\mathcal{K}_2) \partial_\theta \mathcal{K}_1}{\sin^2(E)}, \quad (\text{B.2})$$

where $E = \arccos[\cos(\mathcal{K}_1)\cos(\mathcal{K}_2)]$, $\mathcal{K}_1 = K_1 \cos \theta$ and $\mathcal{K}_2 = K_2 \sin \theta$.

In our calculation example, we fix K_2 at 0.5π and scan K_1 from 0.1π to 1000π . The results of ($W_0 = \frac{W_1+W_2}{2}$, $W_\pi = \frac{W_1-W_2}{2}$) are presented in Fig. B.1. It is clearly seen that both winding numbers (W_0, W_π) grow linearly with the increase of kicking strength K_1 .

Appendix C: Calculation of the mean chiral displacement

In this appendix, we present derivation details of the mean chiral displacement given by Eq. (24) of the main text (see also Refs. [58, 59]). For the ORDKRS, A time-frame independent expression of the mean chiral displacement is given by

$$C(t) = \langle 0| \otimes \langle F| \hat{U}^{-t}(\hat{n} \otimes \sigma_z) \hat{U}^t |0\rangle \otimes |F\rangle, \quad (\text{C.1})$$

where $|0\rangle$ denotes the 0-momentum eigenvector and $|F\rangle$ ($F = 1, 2$) denotes the eigenvector of hyperfine level F . Note that for our choice of initial state, $C(t = 0) = 0$ and $C(t)$ indeed represents a *displacement* over t driving periods. Writing \hat{n} in momentum representation as $\hat{n} = \sum_n n|n\rangle\langle n|$, we have

$$C(t) = \sum_n n \langle 0| \otimes \langle F| \hat{U}^{-t}|n\rangle\langle n| \otimes \sigma_z \hat{U}^t |0\rangle \otimes |F\rangle, \quad (\text{C.2})$$

Expanding \hat{U}^t in position representation as $\hat{U}^t = \sum_\theta |\theta\rangle\langle \theta| U^t(\theta)$, we further obtain

$$C(t) = \sum_{\theta, \theta'} \sum_n n \langle 0|\theta\rangle\langle \theta'|0\rangle\langle \theta|n\rangle\langle n|\theta'\rangle \times \langle F| U^{-t}(\theta) \sigma_z U^t(\theta') |F\rangle. \quad (\text{C.3})$$

Under periodic boundary conditions, we have the following Fourier transforms between position and momentum basis:

$$|\theta\rangle = \frac{1}{\sqrt{N}} \sum_n e^{i\theta n} |n\rangle, \quad |n\rangle = \frac{1}{\sqrt{N}} \sum_\theta e^{-i\theta n} |\theta\rangle, \quad \langle n|\theta\rangle = \frac{1}{\sqrt{N}} e^{i\theta n}, \quad (\text{C.4})$$

where $n = -\frac{N}{2}, -\frac{N}{2} + 1, \dots, \frac{N}{2} - 1$ with $|n\rangle = |n + N\rangle$ and $\theta = \frac{-N\pi}{N}, \frac{-(N-1)\pi}{N}, \dots, \frac{(N-1)\pi}{N}$ with $|\theta\rangle = |\theta + 2\pi\rangle$. Using these relation, we can write $C(t)$ as

$$C(t) = \frac{1}{N} \sum_{\theta, \theta'} \frac{1}{N} \sum_n n e^{i(\theta' - \theta)n} \langle F| U^{-t}(\theta) \sigma_z U^t(\theta') |F\rangle. \quad (\text{C.5})$$

Noting that

$$\frac{1}{N} \sum_n n e^{i(\theta' - \theta)n} = i\partial_\theta \left[\frac{1}{N} \sum_n e^{i(\theta' - \theta)n} \right] = i\partial_\theta \delta_{\theta\theta'}, \quad (\text{C.6})$$

the expression of $C(t)$ reduces to

$$C(t) = \frac{1}{N} \sum_{\theta, \theta'} i\partial_\theta \delta_{\theta\theta'} \langle F| U^{-t}(\theta) \sigma_z U^t(\theta') |F\rangle. \quad (\text{C.7})$$

To proceed, we need to transform the summation over θ, θ' to integrals by taking the number of unit cells $N \rightarrow \infty$. In this limit, we have $\delta_{\theta\theta'} \rightarrow \frac{2\pi}{N} \delta(\theta - \theta')$, $\sum_{\theta, \theta'} \rightarrow N^2 \int_{-\pi}^{\pi} \frac{d\theta}{2\pi} \int_{-\pi}^{\pi} \frac{d\theta'}{2\pi}$, and therefore

$$C(t) = \int_{-\pi}^{\pi} \frac{d\theta}{2\pi} \int_{-\pi}^{\pi} \langle F| U^{-t}(\theta) \sigma_z U^t(\theta') |F\rangle [i\partial_\theta \delta(\theta - \theta')] d\theta'. \quad (\text{C.8})$$

Sending $i\partial_\theta \rightarrow -i\partial_{\theta'}$, performing an integration by parts over θ' and then integrating out θ' , we are left with

$$C(t) = \int_{-\pi}^{\pi} \frac{d\theta}{2\pi} \langle F| U^{-t}(\theta) \sigma_z i\partial_\theta U^t(\theta) |F\rangle. \quad (\text{C.9})$$

According to our discussion in appendix A, $U^t(\theta)$ can be expressed as

$$U^t(\theta) = e^{-iE(\theta)\mathbf{n}(\theta)\cdot\sigma} = \cos(Et) - i \sin(Et)\mathbf{n} \cdot \sigma = [U^{-t}(\theta)]^\dagger, \quad (\text{C.10})$$

where $\mathbf{n} = (n_x, n_y)$ represents the unit vector in any chiral symmetric time frame, and $\sigma = (\sigma_x, \sigma_y)$. Using this expression of $U^t(\theta)$, the operator $U^{-t}(\theta) \sigma_z i\partial_\theta U^t(\theta)$ yields:

$$\begin{aligned} & U^{-t}(\theta) \sigma_z i\partial_\theta U^t(\theta) \\ &= it \cos(2Et) (\partial_\theta E) (n_x \sigma_y - n_y \sigma_x) \\ &+ i \sin(Et) \cos(Et) \partial_\theta (n_x \sigma_y - n_y \sigma_x) \\ &- it [\partial_\theta \sin^2(Et)] \sigma_z \\ &+ \sin^2(Et) (n_x \partial_\theta n_y - n_y \partial_\theta n_x). \end{aligned} \quad (\text{C.11})$$

Next, we note that the hyperfine basis $|F = 1, 2\rangle$ has the following vector expressions:

$$|F = 1\rangle = \begin{pmatrix} 1 \\ 0 \end{pmatrix} \quad |F = 2\rangle = \begin{pmatrix} 0 \\ 1 \end{pmatrix}. \quad (\text{C.12})$$

This means that under the average $\langle F| \dots |F\rangle$, only diagonal elements of the matrix $U^{-t}(\theta) \sigma_z i\partial_\theta U^t(\theta)$ could survive. Furthermore, the term $\partial_\theta \sin^2(Et)$ vanishes after integrating over θ due to the periodicity of E in θ . So we are only left with the last term of Eq. (C.11) under the θ -integral, *i.e.*,

$$C(t) = \int_{-\pi}^{\pi} \frac{d\theta}{2\pi} \sin^2(Et) (n_x \partial_\theta n_y - n_y \partial_\theta n_x). \quad (\text{C.13})$$

Notably, this result is independent of the initial choice of hyperfine level $|F\rangle$. Finally, with $\sin^2(Et) = \frac{1 - \cos(2Et)}{2}$, we arrive at

$$C(t) = \frac{W}{2} - \int_{-\pi}^{\pi} \frac{d\theta}{2\pi} \frac{\cos(2Et)}{2} (n_x \partial_\theta n_y - n_y \partial_\theta n_x) \quad (\text{C.14})$$

where W is the winding number in any chiral symmetric time frame, as given by Eq. (20) of the main text. More specifi-

cally, for the ORDKRS studied in this work, we have:

$$C_1(t) = \frac{W}{2} - \int_{-\pi}^{\pi} \frac{d\theta}{2\pi} \frac{\cos(2Et)}{2 \sin^2(E)} \\ \times [\sin(\mathcal{K}_1) \partial_{\theta} \mathcal{K}_2 - \sin(\mathcal{K}_2) \cos(\mathcal{K}_1) \cos(\mathcal{K}_2) \partial_{\theta} \mathcal{K}_1], \quad (\text{C.15})$$

$$C_2(t) = \frac{W}{2} - \int_{-\pi}^{\pi} \frac{d\theta}{2\pi} \frac{\cos(2Et)}{2 \sin^2(E)} \\ \times [\sin(\mathcal{K}_1) \cos(\mathcal{K}_1) \cos(\mathcal{K}_2) \partial_{\theta} \mathcal{K}_2 - \sin(\mathcal{K}_2) \partial_{\theta} \mathcal{K}_1], \quad (\text{C.16})$$

where $E = \arccos[\cos(\mathcal{K}_1) \cos(\mathcal{K}_2)]$, $\mathcal{K}_1 = K_1 \cos \theta$ and $\mathcal{K}_2 = K_2 \sin \theta$.

-
- [1] P. Leboeuf, J. Kurchan, M. Feingold, and D. P. Arovas, Phys. Rev. Lett. **65**, 3076 (1990).
- [2] G. Casati, B.V. Chirikov, F.M. Izrailev and J. Ford, in *Stochastic Behaviour in classical and Quantum Hamiltonian Systems*, Vol. **93** of Lecture Notes in Physics, edited by G. Casati and J. Ford (Springer, New York, 1979).
- [3] G. Casati and B. V. Chirikov, *Quantum Chaos: Between Order and Disorder* (Cambridge University Press, New York, 1995).
- [4] H. Ammann, R. Gray, I. Shvarchuck, and N. Christensen, Phys. Rev. Lett. **80**, 4111 (1998); B. G. Klappauf, W. H. Oskay, D. A. Steck, and M. G. Raizen, Phys. Rev. Lett. **81**, 1203 (1998).
- [5] Y. Chen and C. Tian, Phys. Rev. Lett. **113**, 216802 (2014); C. Tian, Y. Chen, and J. Wang, Phys. Rev. B **93**, 075403 (2016).
- [6] J. Chabé, G. Lemarié, B. Grémaud, D. Delande, P. Szriftgiser, and J. C. Garreau, Phys. Rev. Lett. **101**, 255702 (2008).
- [7] D. H. White, S. K. Ruddell, and M. D. Hoogerland, Phys. Rev. A **88**, 063603 (2013).
- [8] C. Ryu, M. F. Andersen, A. Vaziri, M. B. d'Arcy, J. M. Grossman, K. Helmerson, and W. D. Phillips, Phys. Rev. Lett. **96**, 160403 (2006); I. Talukdar, R. Shrestha, and G. S. Summy, Phys. Rev. Lett. **105**, 054103 (2010).
- [9] F. L. Moore, J. C. Robinson, C. F. Bharucha, B. Sundaram, and M. G. Raizen, Phys. Rev. Lett. **75**, 4598 (1995); J. F. Kanem, S. Maneshi, M. Partlow, M. Spanner, and A. M. Steinberg, Phys. Rev. Lett. **98**, 083004 (2007); A. Ullah and M. D. Hoogerland, Phys. Rev. E **83**, 046218 (2011).
- [10] F. M. Izrailev, Phys. Rep. **196**, 299 (1990); M. G. Raizen, Advances In Atomic, Molecular, and Optical Physics **41**, 43 (1999); I. Dana, Can. J. Chem. **92**, 77 (2014); M. Sadgrovea and S. Wimberger, Advances in Atomic, Molecular, and Optical Physics **60**, 315 (2011).
- [11] J. Wang and J. B. Gong, Phys. Rev. A **77**, 031405 (2008); J. Wang, A. S. Mouritzen, and J. Gong, J. Mod. Optics **56**, 722 (2009).
- [12] D. R. Hofstadter, Phys. Rev. B **14**, 2239 (1976).
- [13] D. Y. H. Ho and J. Gong, Phys. Rev. Lett. **109**, 010601 (2012).
- [14] T. Geisel, R. Ketzmerick, and G. Petschel, Phys. Rev. Lett. **67**, 3635 (1991); R. Ketzmerick, G. Petschel, and T. Geisel, Phys. Rev. Lett. **69**, 695 (1992).
- [15] I. Dana, Phys. Lett. A **197**, 413 (1995); I. Dana, Phys. Rev. E **52**, 466 (1995).
- [16] H. Wang, D. Y. H. Ho, W. Lawton, J. Wang, and J. Gong, Phys. Rev. E **88**, 052920 (2013).
- [17] D. Y. H. Ho and J. Gong, Phys. Rev. B **90**, 195419 (2014).
- [18] T. Oka and H. Aoki, Phys. Rev. B **79**, 081406 (2009).
- [19] N. H. Lindner, G. Refael, and V. Galitski, Nat. Phys. **7**, 490 (2011).
- [20] J. P. Dahlhaus, J. M. Edge, J. Tworzydło, and C. W. J. Beenakker, Phys. Rev. B **84**, 115133 (2011).
- [21] T. Kitagawa, T. Oka, A. Brataas, L. Fu, and E. Demler, Phys. Rev. B **84**, 235108 (2011).
- [22] Q.-J. Tong, J.-H. An, J. Gong, H.-G. Luo, and C. H. Oh, Phys. Rev. B **87**, 201109 (2013).
- [23] Á. Gómez-León and G. Platero, Phys. Rev. Lett. **110**, 200403 (2013).
- [24] J. Cayssol, B. Dóra, F. Simon, and R. Moessner, Phys. Status Solidi Rapid Res. Lett. **7**, 101 (2013).
- [25] A. G. Grushin, Á. Gómez-León, and T. Neupert, Phys. Rev. Lett. **112**, 156801 (2014).
- [26] R. Wang, B. Wang, R. Shen, L. Sheng, and D. Y. Xing, Europhys. Lett. **105**, 17004 (2014).
- [27] L. Zhou, H. Wang, D. Y. H. Ho, and J. Gong, Eur. Phys. J. B **87**, 204 (2014).
- [28] P. Titum, N. H. Lindner, M. C. Rechtsman, and G. Refael, Phys. Rev. Lett. **114**, 056801 (2015).
- [29] T.-S. Xiong, J. Gong, and J.-H. An, Phys. Rev. B **93**, 184306 (2016).
- [30] J. Klinovaja, P. Stano, and D. Loss, Phys. Rev. Lett. **116**, 176401 (2016); M. Thakurathi, D. Loss, and J. Klinovaja, Phys. Rev. B **95**, 155407 (2017).
- [31] T. Kitagawa, E. Berg, M. Rudner, and E. Demler, Phys. Rev. B **82**, 235114 (2010).
- [32] L. Jiang, T. Kitagawa, J. Alicea, A. R. Akhmerov, D. Pekker, G. Refael, J. I. Cirac, E. Demler, M. D. Lukin, and P. Zoller, Phys. Rev. Lett. **106**, 220402 (2011).
- [33] A. Kundu and B. Seradjeh, Phys. Rev. Lett. **111**, 136402 (2013).
- [34] R. W. Bomantara, G. N. Raghava, L. Zhou, and J. Gong, Phys. Rev. E **93**, 022209 (2016); R. W. Bomantara and J. Gong, Phys. Rev. B **94**, 235447 (2016).
- [35] M. Lababidi, I. I. Satija, and E. Zhao, Phys. Rev. Lett. **112**, 026805 (2014); Z. Zhou, I. I. Satija, and E. Zhao, Phys. Rev. B **90**, 205108 (2014).
- [36] M. D. Reichl and E. J. Mueller, Phys. Rev. A **89**, 063628 (2014).
- [37] Á. Gómez-León, P. Delplace, and G. Platero, Phys. Rev. B **89**, 205408 (2014).
- [38] M. S. Rudner, N. H. Lindner, E. Berg, and M. Levin, Phys. Rev. X **3**, 031005 (2013); P. Titum, E. Berg, M. S. Rudner, G. Refael, and N. H. Lindner, Phys. Rev. X **6**, 021013 (2016).
- [39] I. C. Fulga and M. Maksymenko, Phys. Rev. B **93**, 075405 (2016).
- [40] H. H. Yap, L. Zhou, J. Wang, and J. Gong, Phys. Rev. B **96**, 165443 (2017).
- [41] H. H. Yap, L. Zhou, C. H. Lee, J. Gong, arXiv:1711.09540 (2017).

- [42] L. Zhou, C. Chen, and J. Gong, *Phys. Rev. B* **94**, 075443 (2016).
- [43] J. K. Asbóth, *Phys. Rev. B* **86**, 195414 (2012). J. K. Asbóth, and H. Obuse, *Phys. Rev. B* **88**, 121406 (2013).
- [44] F. Nathan and M. S. Rudner, *New J. Phys.* **17**, 125014 (2015).
- [45] R. Roy and F. Harper, *Phys. Rev. B* **94**, 125105 (2016); R. Roy and F. Harper, *Phys. Rev. B* **96**, 155118 (2017).
- [46] S. Yao, Z. Yan, and Z. Wang, *Phys. Rev. B* **96**, 195303 (2017).
- [47] See A. Eckardt, *Rev. Mod. Phys.* **89**, 011004 (2017) for a review.
- [48] G. Jotzu, M. Messer, R. Desbuquois, M. Lebrat, T. Uehlinger, D. Greif, and T. Esslinger, *Nature (London)* **515**, 237 (2014); M. Aidelsburger, M. Lohse, C. Schweizer, M. Atala, J. T. Barreiro, S. Nascimbène, N. R. Cooper, I. Bloch and N. Goldman, *Nat. Phys.* **11**, 162 (2015).
- [49] T. Kitagawa, M. A. Broome, A. Fedrizzi, M. S. Rudner, E. Berg, I. Kassal, A. Aspuru-Guzik, E. Demler and A. G. White, *Nat. Commun.* **3**, 882 (2012).
- [50] M. C. Rechtsman, J. M. Zeuner, Y. Plotnik, Y. Lumer, D. Podolsky, F. Dreisow, S. Nolte, M. Segev, and A. Szameit, *Nature (London)* **496**, **196** (2013); W. Hu, J. C. Pillay, K. Wu, M. Pasek, P. P. Shum, and Y. D. Chong, *Phys. Rev. X* **5**, 011012 (2015).
- [51] L. J. Maczewsky, J. M. Zeuner, S. Nolte, and A. Szameit, *Nat. Commun.* **8**, 13756 (2017); S. Mukherjee, A. Spracklen, M. Valiente, E. Andersson, P. Ohberg, N. Goldman, and R. R. Thomson, *Nat. Commun.* **8**, 13918 (2017).
- [52] M. Xiao, G. Ma, Z. Yang, P. Sheng, Z. Q. Zhang, and C. T. Chan, *Nat. Phys.* **11**, 240 (2015); R. Süsstrunk and S. D. Huber, *Science* **349**, 47 (2015); R. Fleury, A. B. Khanikaev and A. Alù, *Nat. Commun.* **7**, 11744 (2016); R. Süsstrunk, P. Zimmermann, and S. D. Huber, *New J. Phys.* **19**, 015013 (2017).
- [53] P. H. Jones, M. M. Stocklin, G. Hur, and T. S. Monteiro, *Phys. Rev. Lett.* **93**, 223002 (2004); C. E. Creffield, G. Hur, and T. S. Monteiro, *Phys. Rev. Lett.* **96**, 024103 (2006).
- [54] I. Dana, V. Ramareddy, I. Talukdar, and G. S. Summy, *Phys. Rev. Lett.* **100**, 024103 (2008); M. Sadgrove, M. Horikoshi, T. Sekimura, and K. Nakagawa, *Phys. Rev. Lett.* **99**, 043002 (2007).
- [55] G. Summy and S. Wimberger, *Phys. Rev. A* **93**, 023638 (2016).
- [56] S. Dadrás, A. Gresch, C. Groiseau, S. Wimberger, G. S. Summy, arXiv:1802.08160 (2018).
- [57] Other versions of spin-1/2 kicked rotor were also proposed in R. Scharf, *J. Phys. A: Math. Gen.* **22**, 4223 (1989); M. Thaha, R. Blümel, and U. Smilansky, *Phys. Rev. E* **48**, 1764 (1993); D. R. Masovic, *J. Phys. A: Math. Gen.* **28**, L147 (1995); M. Bienert, F. Haug, and W. P. Schleich, *Phys. Rev. Lett.* **89**, 050403 (2002); C. Zhang, J. Liu, M. G. Raizen, and Q. Niu, *Phys. Rev. Lett.* **92**, 054101 (2004).
- [58] F. Cardano, A. D’Errico, A. Dauphin, M. Maffei, B. Piccirillo, C. de Lisio, G. D. Filippis, V. Cataudella, E. Santamoto, L. Marrucci, M. Lewenstein and P. Massignan, *Nat. Commun.* **8**, 15516 (2017); M. Maffei, A. Dauphin, F. Cardano, M. Lewenstein and P. Massignan, *New J. Phys.* **20**, 013023 (2018).
- [59] E. J. Meier, F. A. An, A. Dauphin, M. Maffei, P. Massignan, T. L. Hughes, and B. Gadway, arXiv:1802.02109 (2018).
- [60] See T. Kitagawa, *Quantum Inf. Process* **11**, 1107 (2012) for a review.
- [61] S. Ryu, A. P. Schnyder, A. Furusaki, and A. W. W. Ludwig, *New J. Phys.* **12**, 065010 (2010); C. Chiu, J. C. Y. Teo, A. P. Schnyder, and S. Ryu, *Rev. Mod. Phys.* **88**, 035005 (2016).
- [62] K. v. Klitzing, G. Dorda, and M. Pepper, *Phys. Rev. Lett.* **45**, 494 (1980).
- [63] R. W. Bomantara and J. Gong, arXiv:1712.09243 (2018).
- [64] See K. Sacha and J. Zakrzewski, *Rep. Prog. Phys.* **81**, 016401 (2018) for a review.
- [65] M. Rodriguez-Vega, and B. Seradjeh, arXiv:1706.05303 (2018).